Primer and Historical Review on Rapid Cardiac CINE MRI

Aaron D. Curtis, BASc,[1,2] and Hai-Ling M. Cheng, PhD[1,2,3]*

Acceleration is an important consideration when imaging moving organs such as the heart. Not only does acceleration enable motion-free scans but, more importantly, it lies at the heart of capturing the dynamics of cardiac motion. For over three decades, various ingenious approaches have been devised and implemented for rapid CINE MRI suitable for dynamic cardiac imaging. Virtually all techniques relied on acquiring less data to reduce acquisition times. Parallel imaging was among the first of these innovations, using multiple receiver coils and mathematical algorithms for reconstruction; acceleration factors of 2 to 3 were readily achieved in clinical practice. However, in the context of imaging dynamic events, further decreases in scan time beyond those provided by parallel imaging were possible by exploiting temporal coherencies. This recognition ushered in the era of *k-t* accelerated MRI, which utilized predominantly statistical methods for image reconstruction from highly undersampled *k*-space. Despite the successes of *k-t* acceleration methods, however, the accuracy of reconstruction was not always guaranteed. To address this gap, MR physicists and mathematicians applied compressed sensing theory to ensure reconstruction accuracy. Reconstruction was, indeed, more robust, but it required optimizing regularization parameters and long reconstruction times. To solve the limitations of all previous methods, researchers have turned to artificial intelligence and deep neural networks for the better part of the past decade, with recent results showing rapid, robust reconstruction. This review provides a comprehensive overview of key developments in the history of CINE MRI acceleration, and offers a unique and intuitive explanation behind the techniques and underlying mathematics.
Level of Evidence: 5
Technical Efficacy Stage: 1

J. MAGN. RESON. IMAGING 2022;55:373–388.

CARDIOVASCULAR DISEASE is the leading cause of death globally, afflicting both sexes and all races and accounting for 31% of all deaths worldwide.[1] The disease encompasses a broad spectrum of conditions, including myocardial infarction, valve stiffening, and viral infection, all of which adversely impact regional tissue and compromise global cardiac function. Regardless of the specific nature of the disease, diagnosis is best performed with a cross-sectional imaging method that captures cardiac structure and dynamic motion. Echocardiography, with its unique real-time imaging capability, is the mainstay for this task, providing an assessment of ejection fraction, left ventricular volume, regional wall motion, and valve dynamics.[2,3] However, factors such as interobserver variability, a limited acoustic window, and poor tissue contrast limit the performance of echocardiography in clinical diagnosis.[4] In particular, poor tissue contrast hampers assessment of tissue-level changes such as perfusion loss, necrosis, and scarring.[4] To fill the gaps left by echocardiography, other imaging modalities, namely, magnetic resonance imaging (MRI), computed tomography (CT), and nuclear medicine, are employed. While these methods have limited real-time capabilities and often require strategies to gate to the cardiac and respiratory cycles,[5] they provide in many instances essential complementary information to

View this article online at wileyonlinelibrary.com. DOI: 10.1002/jmri.27436

Received Jun 10, 2020, Accepted for publication Oct 27, 2020.

*Author reprint requests to: H.-L.M.C., Institute of Biomedical Engineering, University of Toronto, 164 College Street, RS407, Toronto, ON M5S 3G9, Canada. E-mail: hailing.cheng@utoronto.ca

Contract grant sponsor: Queen Elizabeth II Graduate Scholarship in Science & Technology (to A.D.C.); Contract grant sponsor: Natural Sciences and Engineering Research Council of Canada; Contract grant number: 2019-06137 (to H-L.M.C.); Contract grant sponsor: Canada Foundation for Innovation/Ontario Research Fund; Contract grant number: 34038; and a Dean's Spark Professorship from the University of Toronto.

From the [1]The Edward S. Rogers Sr. Department of Electrical and Computer Engineering, University of Toronto, Toronto, Ontario, Canada; [2]Ted Rogers Centre for Heart Research, Translational Biology & Engineering Program, Toronto, Ontario, Canada; and [3]Institute of Biomedical Engineering, University of Toronto, Toronto, Ontario, Canada

Additional supporting information may be found in the online version of this article

echocardiography for a complete diagnosis. Of these modalities, only MRI is free from ionizing radiation and the use of radioactive tracers.

Cardiac MRI can inform on a range of anatomical, functional, and microstructural parameters and does so with unparalleled soft-tissue contrast and high spatial resolution. Myocardial deformations can be observed not only locally but also globally. In addition to global cardiac function, other parameters difficult to obtain on echocardiography can also be assessed accurately, such as perfusion deficits and myocardial remodeling.[6,7] However, cardiac MRI has yet to become a routine part of clinical workup in cardiac patients,[8,9] largely due to one major limitation of MRI: speed. To work around relatively slow acquisitions, strategies have been devised to compensate for the speed of cardiac contraction and motion due to breathing. However, these strategies have limitations when the patient has arrhythmia or cannot breath-hold. Some real-time imaging methods have been developed[10,11,12] over the years; yet real-time MRI is still not widely available. This is due to inherent trade-offs among spatial resolution, temporal resolution, and volume coverage. For this reason, acceleration methods have been intensely studied for nearly three decades. In this article, we provide a historical review of strategies for accelerated cardiac CINE MRI. We begin with established methods such as parallel imaging and conclude with the newest developments rooted in deep learning and artificial intelligence. To understand how each innovation builds on previous ones, we also present intuitive explanations and the underlying signals and systems concepts where relevant. It is important to note that while this review focuses on CINE MRI, many of the acceleration methods to be covered are also relevant for other cardiac applications (eg, perfusion, tagging, relaxometry).

Conventional Cardiac MRI

CINE Imaging

Dynamic cardiac MRI is conventionally performed with a technique known as CINE,[13] which takes its name from cinematography. In brief, a "movie" of a single beating heart cycle is reconstructed by literally stitching together numerous partial datasets from many heartbeats—typically 15–18, more if multiple slices are acquired. Because data acquisition is too slow to collect all data in a single heartbeat, acquisition is segmented over several heartbeats. Specifically, the cardiac cycle is divided into many phases (or timepoints), and the fully sampled *k*-space for each phase is divided into multiple segments (Fig. 1). Once all segments for all cardiac phases are acquired, the data are temporally reordered and converted to the image domain to produce the impression of a continuously acquired time series. One can readily appreciate that this technique does not provide real-time dynamics and works robustly only if cardiac cycles are sufficiently similar. In the presence of arrhythmia or other undesired motion, which is common in patients with heart disease, artifacts will be created in the reconstruction. To resolve this issue, arrhythmic data must be identified, usually via an electrocardiogram (ECG), and rejected by the reconstruction protocol. Depending on the specific implementation of CINE, other more nuanced limitations may also surface.

The most common and robust CINE implementations utilize cardiac gating: prospective or retrospective[14,15] (Fig. 1). A common approach to synchronizing with the sinus rhythm is the placement of ECG probes on the chest. In prospective CINE, data acquisition is synchronized to the patient's ECG signal, notably the "R" wave that reflects depolarization and the onset of left ventricular contraction (systole). This synchronization allows imaging to be performed at defined timepoints throughout the cardiac cycle and guarantees that the same cardiac phases are acquired at every heartbeat. However, imaging pauses for a substantial portion of diastole (20–40% of the end of the cardiac cycle) in preparation for a potential early arrival of the next "R" wave; diastolic function becomes very difficult to assess. On the other hand, retrospective gating acquires data continuously and utilizes the ECG waveform only in the image reconstruction stage. Acquired data are reordered temporally and assigned to "similar" cardiac phases. The full cardiac cycle, from systole to end diastole, is thus captured. To ensure robust temporal reordering, only cardiac cycles of similar temporal length are used in the reordering process; all other data are rejected. Acquisition must be performed until enough data have been acquired to sufficiently fill the entire *k*-space for each cardiac phase.

Today, CINE is mostly performed in two dimensions and under breath-hold. The acquisition time is long and increases significantly with greater spatial resolution, volume coverage, and motion-corrupted acquisitions. Many of the current limitations of CINE, such as lack of 3D coverage, resolution tradeoff, and respiratory motion, can be addressed via acceleration strategies. Below we elaborate on two fundamental limitations.

Fundamental Limitations of Conventional Rapid CINE

COMPLEX CARDIAC MOTION "SIGNATURE" IS IGNORED. The assumption of temporal consistency in the cardiac cycle is difficult to satisfy in healthy people, let alone patients with heart disease who often have arrhythmia or other abnormalities in the sinus rhythm. By retaining only data that are consistent between cardiac cycles, CINE effectively ignores heterogeneity in cardiac dynamics, heterogeneity that may be in and of itself a hallmark of disease.[16]

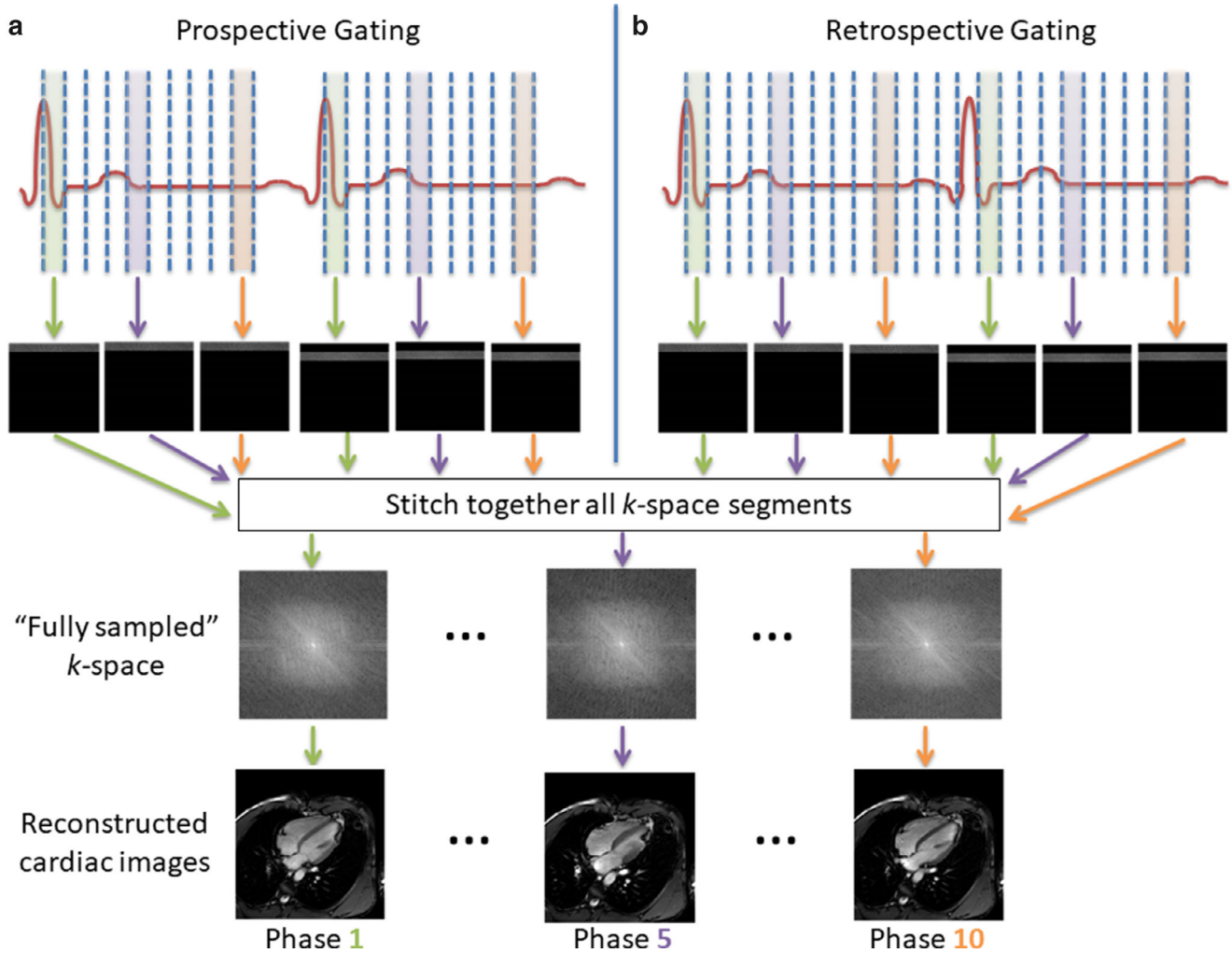

FIGURE 1: CINE imaging. Reconstruction is shown for three example cardiac phases (phase 1, green; phase 5, purple; phase 10, orange). Prospective gating (a) involves precisely synchronized cardiac phases but leaves out late diastole in preparation for the next R-wave. Retrospective gating (b) acquires continuously and allows for slight offsets in the timing of cardiac phases. The full *k*-space at each phase is stitched together from partial acquisitions over many cardiac cycles.

REAL-TIME DYNAMICS ARE ABSENT. Perhaps the greatest limitation of CINE is its failure to capture real-time dynamics. Ideally, all relevant information at every timepoint should be acquired in a single heartbeat. If this can be achieved, heterogeneity in cardiac dynamics will be fully captured. However, attaining true real-time acquisition is very challenging, and using past or future cardiac cycles to infer information for the current cycle, while practical, can introduce gross errors into the reconstruction.

Hardware-Driven Acceleration

Conventional CINE circumvents the challenge of slow acquisition by segmenting the acquisition space, also known as *k*-space. An alternative or complementary method is to use hardware acceleration driven either by acquiring fewer samples of the full *k*-space or altering the *k*-space trajectory. Because *k*-space is essentially the 2D Fourier transform of the image domain, dropping data points or undersampling *k*-space to achieve faster scans naturally introduces artifacts into the reconstructed image. Fortunately, these artifacts are correctable under specific circumstances. The following sections describe the dominant strategies for hardware-driven acceleration and solutions to reduce related artifacts.

Parallel Imaging

Parallel imaging gains speed by employing multiple receiver coils, each individually acquiring fewer lines in *k*-space (eg, only odd lines to scan twice as fast). The speed-up factor is equal to the number of independent receiver coils. Unfortunately, undersampling *k*-space introduces aliasing, or replica copies of the image, across the field-of-view (FOV), overlapping with the main object of interest. Mathematically, this phenomenon is analogous to aliasing of frequency components from undersampling a time-domain signal. To recover the original image, we need to remove the aliasing. We also need to leverage the inherent coil sensitivities, which "illuminate" the image differently, to replace the encoding that is

missing from unacquired *k*-space lines. We discuss the most well-known of these methods: parallel imaging with localized sensitivities (PILS),[17] sensitivity encoding (SENSE),[18] simultaneous acquisition of spatial harmonics (SMASH),[19] and generalized autocalibrating partial parallel acquisition (GRAPPA).[20]

PILS was proposed by Griswold et al in 2000.[17] This method works by taking advantage of the localized sensitivity each receiver coil has over a distinct region of the subject being imaged. Knowing the exact position of each coil in the full FOV, one can then extract for each coil the correct image instance and discard replicas. The full image is obtained by combining different portions of the FOV extracted from different coils. While effective, PILS is limited by strict configurations of the coil array.

SENSE, an image "unfolding" algorithm introduced by Pruessmann et al in 1999,[18] is another technique in which reconstruction takes place in the image domain. Reconstructing from an undersampled *k*-space from each coil yields an aliased image with a partial FOV. These aliased images must be unfolded to produce a full-FOV image. To successfully unfold, one must satisfy two criteria. First, one requires information on coil sensitivities to assign aliased image pixels to the correct unfolded spatial location. Second, reconstructed full-FOV images from all coils must be combined to produce the final image. SENSE is currently one of the most widely used parallel imaging methods (Fig. 2).

SMASH was introduced by Sodickson and Manning in 1997.[19] Each *k*-space line is simultaneously acquired by N receiver coils. Using coil sensitivities, each acquired *k*-space line may be decomposed into N individual *k*-space lines, thereby recovering the full *k*-space. Note that, unlike SENSE, SMASH operates on *k*-space, not images. In 2002, Griswold et al refined this technique and published GRAPPA.[20] Like PILS, GRAPPA uses local coil sensitivities, which are estimated by comparing acquired *k*-space lines against designated autocalibration signal (ACS) lines near the center of *k*-space. This comparison procedure is analogous to SMASH and is an extension of VD-AUTO-SMASH.[21] Using these local sensitivities, GRAPPA recovers a set of single-coil images, which can be combined using a magnitude reconstruction procedure to recover the fully sampled image. GRAPPA is superior for heterogeneous anatomies such as the abdomen and for small FOV applications.

Non-Cartesian Acquisition Trajectories

A different approach to accelerating data acquisition is to traverse *k*-space using a non-Cartesian trajectory through the central region of *k*-space. The premise is that certain regions of *k*-space contain significantly more useful information regarding cardiac structure and dynamics. Our first example is the work of Winkelmann et al, who proposed golden-angle radial undersampling to sample the low spatial frequency of the *k*-space region more densely.[22] This approach is implemented by traversing different linear trajectories through *k*-space separated by 111.25°, an angle chosen to minimize overlap between various spokes (ie, maximize spacing). These trajectories are iteratively sampled until approximately the

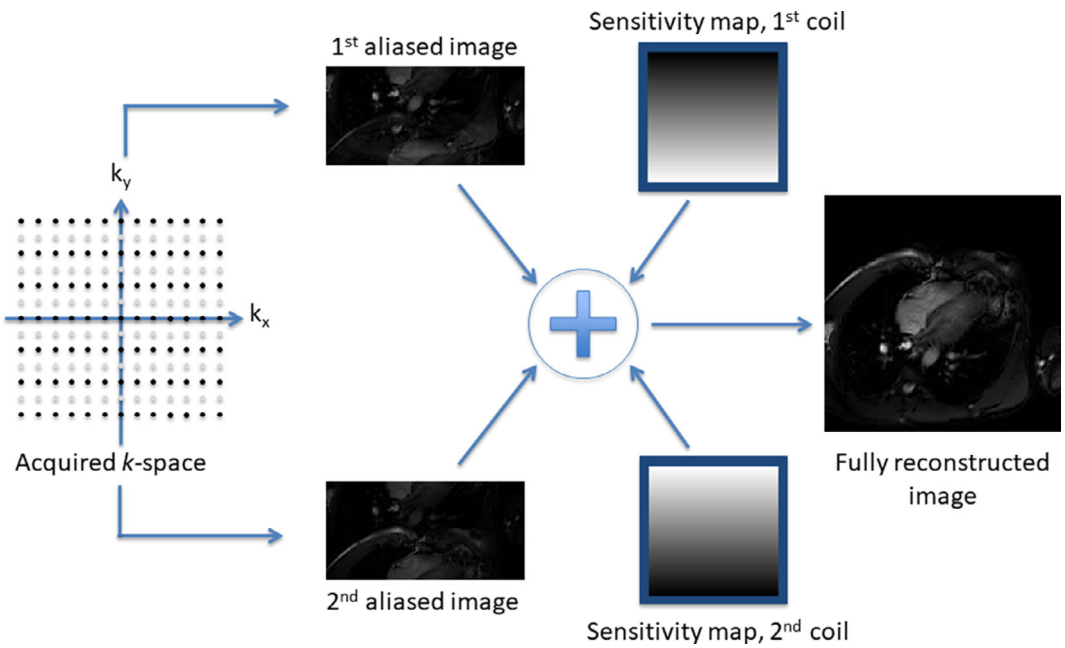

FIGURE 2: SENSE parallel imaging. This example illustrates SENSE imaging with two coils, where alternating *k*-space lines are acquired. Reconstructed images are aliased due to skipping alternate lines in *k*-space. The aliased images are unfolded, given information on the associated coil sensitivity maps, to produce a final, unaliased reconstructed image. Note: sensitivity maps shown are illustrative only.

entire *k*-space has been covered. By constantly resampling the center of *k*-space, one can account for changes in dynamic image contrast. For this reason, golden-angle radial sampling is beneficial for accelerated MRI.[23]

To sample the contrast-rich central region of *k*-space more frequently, the golden-angle radial acquisition approach traded off capturing with high fidelity the outer regions of *k*-space. To address this limitation, Prieto et al proposed acquiring multiple spirals that traverse zero frequency, where the separation between spirals is defined by the golden ratio.[24] Essentially, by transforming spokes into spirals, these authors were able to adapt to dynamic motion without incurring a significant compromise in reconstructed image quality.

k-t Accelerated Imaging

Thus far, we have examined acceleration approaches that exploit correlations in *k*-space only. Dynamic datasets, however, have an extra time dimension, which we need to consider in maximizing acceleration. In other words, we must exploit correlations in both *k*-space and time: this is the unifying concept at the heart of accelerated dynamic MRI. In the presence of "missing" acquired data in *k-t* space, *k-t* acceleration reduces the reconstruction problem to a mathematical estimation via a linear combination of acquired points in *k-t* space:

$$\hat{x}_n = w_{1,n}k_1 + w_{2,n}k_2 + \ldots + w_{m,n}k_m \qquad (1)$$

where $\hat{x}_n$ is the n^{th} point in the full reconstruction, k_i is the i^{th} acquired point, and $w_{i,n}$ is the weight associated with k_i. Please note that this equation is not specific to *k-t* accelerated imaging. Other techniques such as SENSE and GRAPPA use Eq. 1 in their reconstruction procedures.

In *k-t* accelerated imaging, successful implementation of Eq. 1 requires two design decisions. First, one must choose a reconstruction domain for the full reconstruction, $\hat{x}_n$, which is what we are trying to estimate (eg, an image). Second, one must choose the weights, $w_{i,n}$, for the linear combination of acquired points k_i. The weights indicate the utility of each acquired point in the reconstruction.

Reconstruction Domains: x-t *and* x-f *Space*

Although MRI data are acquired in only one domain, namely, *k-t* space, there are typically two choices for the reconstruction domain: *x-t* and *x-f* space. The *x-t* space is derived by taking the inverse spatial 2D Fourier transform at each time index in *k-t* space, yielding a time series of 2D spatial-domain images. The *x-f* space is derived from *x-t* space by mathematically transforming the temporal axis via a 1D Fourier transform. While the most common approach is the Fourier transform, additional approaches may be applied.

There is one notable exception to reconstructing in either *x-t* or *x-f* space. As we shall revisit in greater detail shortly, *k-t* GRAPPA[25] uses neither; instead, it uses *k-t* space for both acquisition and reconstruction.

Linear Combinations: Constructing the Filter

Next, one must choose filter weights for the linear combination; this can be done in one of two ways. The first method is to apply direct filtering on *k-t*, *x-t*, or *x-f* space. Direct filtering, which is a linear process involving convolution, is straightforward to implement but is incapable of handling complex motion artifacts. The second method is statistical linear combination. With this approach, the weights are determined *directly* from autocorrelation and cross-correlation, which are mathematical measures of similarity among acquired points, or between acquired and fully reconstructed points, respectively. Similarity may be used to judge significance, because two dissimilar points provide more information and are, hence, more significant than two similar points. Thus, the statistical approach relies on the fact that some acquired points carry greater significance and are more useful in estimating the full reconstruction. The following sections delve into the inner workings of these linear methods.

DIRECT FILTERING. A few cardiac MRI approaches belong to the direct filtering category. The earliest example is MR fluoroscopy, introduced in 1988.[26] This technique utilizes a "sliding window" to interpolate the full *k-t* space, where missing data points are estimated using a 1D filter along the temporal direction with filter weights all equal to one. This type of moving average filter effectively repeats an acquired data point to other timepoints where data are missing. The more missing data points or time frames where 2D *k*-space was not acquired, the faster the acquisition but the more filter weights required for interpolation. However, this comes at a cost of poorer reconstruction fidelity, particularly if the tissue is nonstationary. Nonetheless, the sliding window filter is a simple example for understanding how filtering can be used to interpolate missing data.

Another direct filtering method was introduced in 1999: unaliasing by Fourier-encoding the overlaps in the temporal dimension (UNFOLD).[27] Alternate phase-encode lines are acquired at each timepoint, first the odd-indexed lines, then the even-indexed, and so forth. Aliased replicas appear in the corresponding images due to skipping lines in *k*-space, and a linear phase shift will arise in these images as a result of the alternating sampling pattern (Fig. 3). Note that the central component of each image remains unaffected and has zero phase shift, whereas the aliased replicas in each image are labeled with a characteristic phase shift dependent on the time of sampling. This phase shift in the aliased replicas as a function of time is equivalent to a frequency shift in the Fourier spectrum; the central component, however, remains at zero frequency. We can avail this spectral separation and eliminate the replicas by first converting *x-t* space into *x-f*

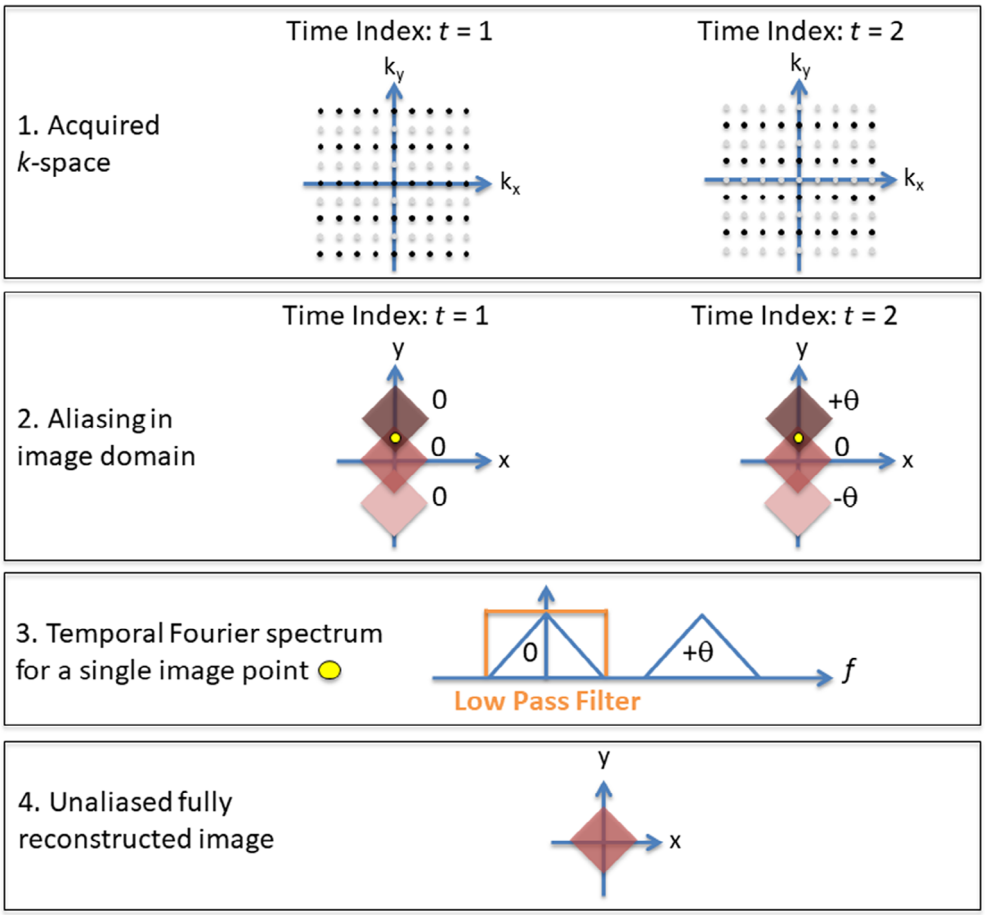

FIGURE 3: UNFOLD imaging. Alternate phase encode lines are acquired at successive time indices. The phase encode line skipping introduces aliasing in reconstructed images, while the alternation introduces a phase shift θ in the aliased replicas (the baseband image does not undergo a phase shift). If we were to take one point in the image (yellow dot) and apply a temporal Fourier transform, we will observe that the phase shift in the image domain is equivalent to a frequency shift in the temporal Fourier transform. We can apply a low-pass filter to recover only the baseband spectrum and reconstruct a full unaliased image.

space by applying a temporal Fourier transform and then lowpass filtering along the *f*-axis to extract only the central component, thereby obtaining a fully reconstructed image. Although more complex than the sliding window, UNFOLD is simply 1D filtering in *x-f* space.

Our last example is *k-t* GRAPPA,[25] a variation of GRAPPA parallel imaging that incorporates *k-t* acceleration. In the first step, each missing data point in *k-t* space is individually assigned to a subset of the acquired *k-t* space data. Each subset is composed of acquired data points associated with a similar time index as the missing data point. The acquired data points in each subset are then used to compute an initial estimate for the corresponding missing data point. In the second step, the GRAPPA protocol is applied to each subset to compute a secondary estimate of the missing data points. Both of these estimates of *k-t* space use linear combinations, where the weights are determined from the acquired ACS lines. The results of these two combinations are then added together to yield a fully interpolated *k-t* space. While *k-t* GRAPPA improves the overall signal-to-noise ratio (SNR), it also exacerbates artifacts, a consequence of using only a small subset of acquired *k-t* data. This issue, as seen in the next section, may be addressed via statistical filtering.

In summary, direct filtering was a useful technique in the early stages of dynamic MRI research. It demonstrated the reconstruction capabilities of linear estimation using acquired *k-t* space data. However, direct filtering is no longer widely used and has been replaced with a more robust form of linear estimation: statistical linear combinations.

STATISTICAL LINEAR COMBINATIONS. As demonstrated above, direct filtering uses the entire *k-t* space (MR fluoroscopy, UNFOLD) or local *k-t* space points (*k-t* GRAPPA) to determine the appropriate weights for estimating the full reconstruction. The direct filtering approach is limited, as it does not consider the individual significance of acquired *k-t* space points. This is resolved through statistical linear combination.

Statistical linear combination computes a full reconstruction using three primary steps. The first step is

computing an initial guess, which is an arbitrary estimate of what the full reconstruction should be (eg, all zeros). The second step is to judge the accuracy of our initial guess by computing the error between our initial guess and the acquired data. This is performed by converting the initial guess to the acquisition domain and directly comparing it to the acquired *k-t* space. The third step is to use these errors to update each individual point in our initial guess, thereby obtaining the full reconstruction. Each update consists of a unique linear combination of all the error terms calculated in step two, where every weight is chosen to be a product of the autocorrelation and cross-correlation terms associated with a particular error term. This effectively rescales each error term based on the significance of the corresponding point in the acquisition domain, as well as the usefulness of the corresponding point in estimating a point in the full reconstruction. The result of these statistical linear combinations is then added to the initial guess, thereby facilitating the updates mentioned previously. Mathematically, this entire procedure can be represented by the following equation:

$$\underline{\hat{x}} = x_0 + MF^H E^H \left(EFMF^H E^H + \Psi\right)^{\dagger} (\underline{k} - F(x_0)) \qquad (2)$$

where $\underline{\hat{x}}$ is the full reconstruction, x_0 is an initial guess of the full reconstruction (if available), $\underline{k}$ is the acquired *k-t* space data, E is the undersampling mask, F is the relationship between the reconstruction domain (*x-t* or *x-f*) and the acquisition domain (*k-t*), and Ψ is noise in the acquired data. The matrix M is the autocorrelation of the unaliased training data, which is a set of low-resolution, unaliased images emphasizing the central *k*-space region (eg, previously acquired fully sampled CINE scan). The autocorrelation and cross-correlation of the acquired data are, respectively, $(EFMF^H E^H + \Psi)^{\dagger}$ and $MF^H E^H$. In Eq. 2, † denotes a pseudoinverse, which protects against inaccuracies in the autocorrelation. These inaccuracies arise from unforeseen errors in the training scan or unforeseen errors in the acquisition data. A summary of Eq. 2 can be found in Table 1. A full derivation of Eq. 2 can be found in the Appendix S1.

Mathematically, Eq. 2 is called the Bayesian Gauss-Markov Theorem. Rosenfeld provides an in-depth mathematical derivation for those who are interested.[28] More common, however, is the name Wiener filter, dedicated to Norbert Wiener, a pioneer in linear minimum mean square error (LMMSE) estimation. The Wiener filter is the workhorse of *k-t* accelerated imaging, as we shall show next.

k-t *BLAST and* k-t *SENSE*

Among the linear estimators used for *k-t* acceleration, *k-t* BLAST and *k-t* SENSE are often considered the standard, particularly when it comes to evaluating new technological advances.[29] Developed by Tsao et al in 2003, *k-t* BLAST and *k-t* SENSE both use Wiener filtering to estimate missing data (via Eq. 2), with the incorporation of coil sensitivities in the equation for *k-t* SENSE. The reconstruction domain is defined as a slice in *x-f* space, the observed data as a slice in *k-t* space (ie, at a fixed k_x), M as the autocorrelation information of *x-f* space, E as a downsampling matrix, F as a 2D Fourier transform to convert a slice in *x-f* space to a slice in *k-t* space, and Ψ as the autocorrelation of measurement noise. Baseline data are defined as the static image component, ie, a slice in *x-f* space with all terms $f \neq 0$ set to zero. To compute this baseline, all observed *k-t* space data are used to create a temporally averaged *k*-space, which is then used to initialize *x-f* space at $f = 0$. The *k-t* BLAST algorithm is shown in Fig. 4.

When parallel imaging is added to *k-t* BLAST, the estimation is modified to include a coil sensitivity-encoding matrix S. The matrix S can be combined with the downsampling matrix E to create a new matrix that is used in place of E in Eq. 2, yielding *k-t* SENSE. Both *k-t* BLAST and *k-t* SENSE achieve improved reconstruction quality compared to previous results and permit an acceleration factor of 4.

TABLE 1. Parameters in the Reconstruction Equation for *k-t* Accelerated Imaging

Term	Representation	Meaning
$\underline{\hat{x}}$	Full reconstruction	An example would be a reconstructed image from an undersampled dataset
x_0	Baseline data	An initial guess for $\underline{\hat{x}}$. Exists in the same domain as $\underline{\hat{x}}$.
$C = MF^H E^H$	Cross-correlation	Similarities between acquired points and fully reconstructed points
$A^{\dagger} = (EFMF^H E^H + \Psi)^{\dagger}$	Autocorrelation	Similarities among acquired points. *Includes* noise Ψ.
$\underline{k} - F(x_0)$	Error in baseline data	The error in our initial guess of $\underline{\hat{x}}$

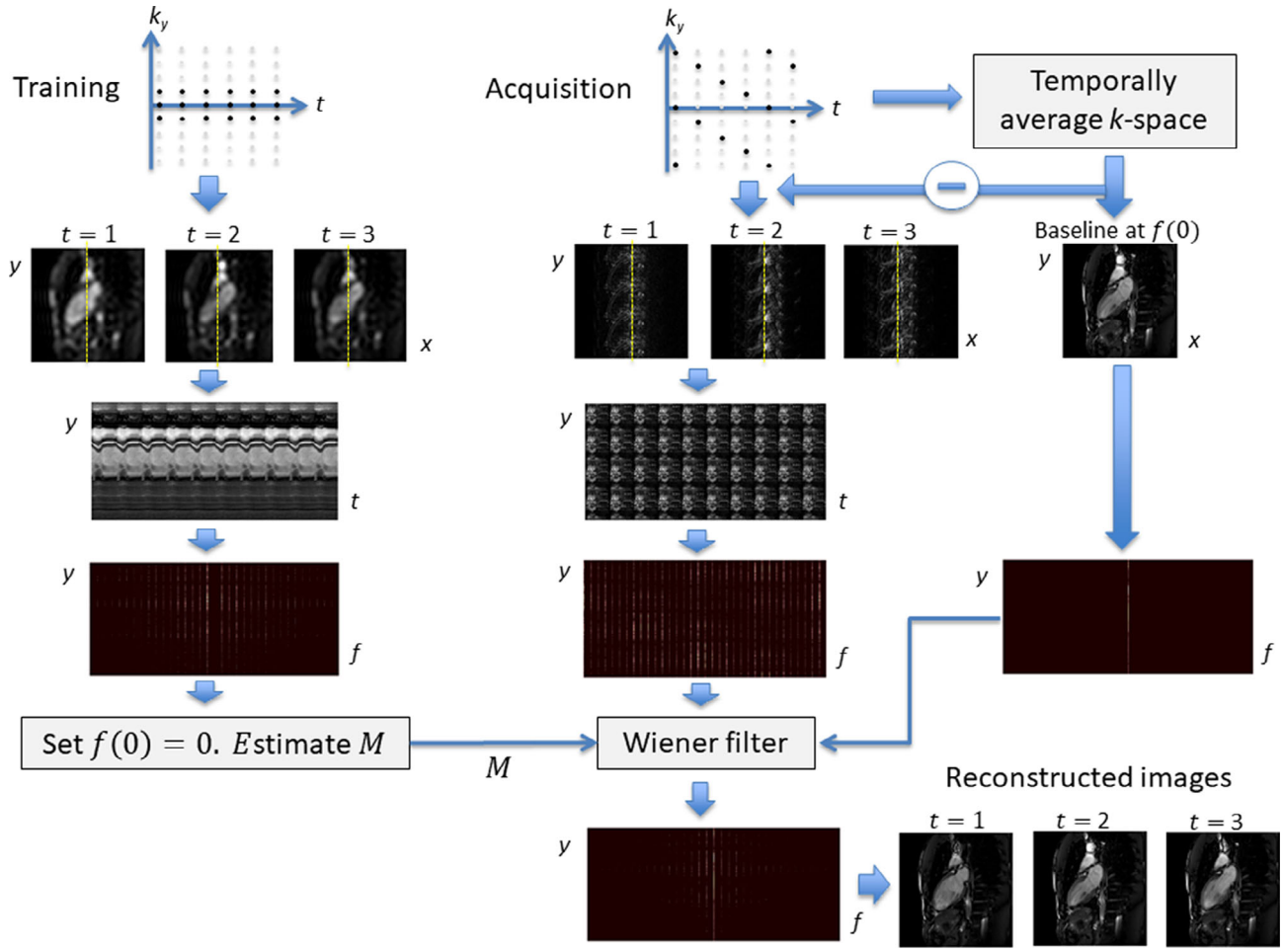

FIGURE 4: ***k-t*** **BLAST imaging. This acceleration technique is divided into two stages. In the training stage, central** ***k*****-space is acquired rapidly to produce a time-series of low-resolution images of the heart. We then sample along one line in the image domain (yellow dotted line) and view its temporal variation in the** ***y-t*** **domain. A 1D temporal Fourier transform is applied to yield a** ***y-f*** **map, from which we remove the central DC, ie,** ***f*****(0), component before estimating the autocorrelation matrix** ***M*****. During acquisition,** ***k*****-space is acquired in an interleaved fashion as shown (black: acquired points; gray: skipped points), producing aliasing in the reconstructed images. Following the same procedure as for training data, we obtain a** ***y-f*** **map that clearly reveals aliasing in a diagonal spatiotemporal direction. This can be seen in the relatively equal strength of diagonally aliased** ***y-f*** **space frequency bands. At the same time, a baseline image is estimated by temporally averaging together acquired** ***k*****-space so as to remove aliasing. This baseline estimate is compared to the acquired data during Wiener filtering, which uses the estimated matrix** ***M*** **from training. The final output is an unalised** ***y-f*** **domain, which is inverse Fourier transformed to produce full reconstructed images. Note: the subtraction, or comparison, between undersampled acquired data and the baseline estimate is performed within the Wiener filter; we have shown the subtraction explicitly outside the Wiener filter box for clarity.**

k-t *PCA*

When aliasing in *x-f* space is modest, *k-t* BLAST and *k-t* SENSE perform well. However, if there is broad temporal bandwidth due to the presence of rapidly moving content in the MR images, minimal acceleration is to be gained. To achieve higher acceleration under these circumstances, Pedersen et al proposed *k-t* PCA/SENSE as an extension of *k-t* BLAST/SENSE.[30] This method makes use of principal component analysis (PCA) to represent temporal frequency data using a few basis functions known as principal components. Specifically, instead of representing an *x-f* profile as a decomposition onto many temporal Fourier frequencies with nonnegligible weights, the *x-f* profile is alternatively represented as a linear combination of predetermined principal components, each with a defined spectral characteristic. Since very few weights associated with nonnegligible principal components are retained, and since the temporal spectrum of the principal components are fixed, separation of aliased signals is greatly facilitated, thus enabling higher acceleration factors than *k-t* BLAST, up to 8.

Summary

k-t accelerated imaging is considered one of the earlier approaches to accelerate cardiac MRI. By exploiting not only spatial but also temporal coherencies, *k-t* acceleration methods solved a primary shortcoming of conventional parallel imaging: limited acceleration. Unfortunately, *k-t* methods are susceptible to reconstructing erroneous images in the

absence of global information. This is a tradeoff from using autocorrelation functions, which favor similarities among local pixels over distant ones. To capture and utilize global similarities for ensuring reconstruction accuracy, an alternate method is needed. Compressed sensing solves this precise dilemma.

Compressed Sensing

Compressed sensing is a signal processing method for recovering a signal from far fewer samples than dictated by the Nyquist–Shannon sampling theorem. Three criteria must be met: 1) the signal must be sparse (ie, compressible) in some transform domain Ψ; 2) the signal must possess incoherent artifacts from random undersampling; and 3) the signal must undergo nonlinear reconstruction that enforces both data consistency and sparsity.

The first criterion of transform sparsity is a topic of ongoing research. Sparsity transforms allow us to represent images using a fewer number of data points. Thus, they are a representation of the most important information across the *entire* image (Fig. 5). Effectively, a sparsifying transform achieves two things: a high degree of compression and a global representation that regularizes our full reconstruction and ensures accurate reconstruction of an image.

The second criterion of incoherence involves sampling *k*-space such that we have incoherent artifacts. Truly random sampling of *k*-space would yield very low coherence but is also impractical. Sampling trajectories must follow smooth curves and cannot involve excessively rapid switching of gradients that, even if implementable, would induce eddy currents and peripheral nerve stimulation. Furthermore, the central region of *k*-space is spectrally dense; this asymmetry must be balanced against purely random sampling throughout *k*-space. To resolve these issues, a pseudorandom acquisition undersampling strategy is used. Examples of pseudorandom sampling strategies are discussed throughout the remainder of this section.

The third criterion of nonlinear reconstruction involves finding an inverse solution within the constraints of data consistency and sparsity. Given an observed signal k in k-space, which is the output of our system E, we want to determine the input signal x (in our case, an MR image)—ie, $k = Ex$. The system E accounts for the Fourier transform and the pseudorandom sampling mask. To find the inverse solution, we formulate the following regularized optimization:

$$\hat{x} = \underset{x}{\operatorname{argmin}} \|Ex - k\|_2^2 + \lambda \Phi(x) \qquad (3)$$

We estimate a reconstructed image $\hat{x}$ by minimizing a data consistency term $\|Ex - k\|_2^2$, where x is the image iteratively updated by the optimization. This data consistency term ensures the reconstruction agrees with acquired k-t space data. The second part of Eq. 3 contains the regularization term, $\Phi(x)$, which stabilizes the solution, and a scalar λ that

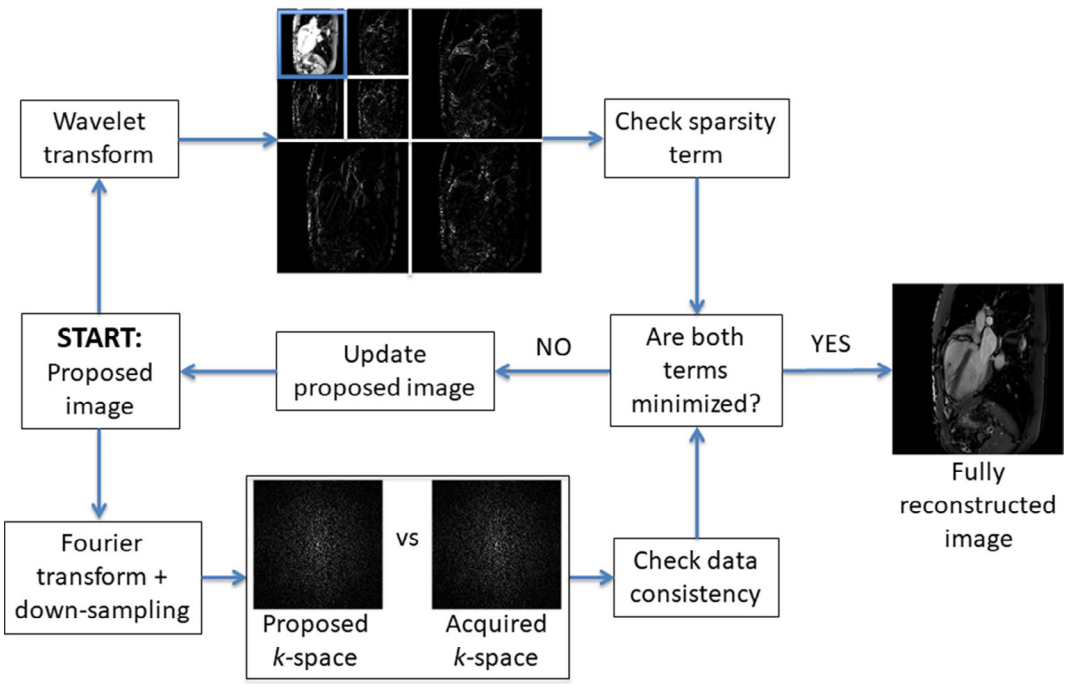

FIGURE 5: Compressed sensing. The protocol begins with a proposed image, which is checked for both sparsity and data consistency. The wavelet transform has excellent sparsifying properties and compactly represents the entire image in a low-resolution version (blue box); the rest of the domain are high-resolution details at two resolution levels. In addition to ensuring a globally consistent reconstruction through sparsity, the optimization loop also checks for data consistency by minimizing the error between acquired *k*-space and that from the proposed image.

controls the degree of regularization to avoid overfitting. In compressed sensing, the regularization term is replaced by the l_1 norm on the transform Ψ to enforce sparsity (note: l_1 is used instead of the l_0 norm, which is challenging to evaluate). In cardiac applications, Ψ has taken the form of the temporal discrete cosine transform, spatiotemporal wavelets, and spatiotemporal total variation.

To gain greater intuition into the sparsity constraint in Eq. 3, let us assume that Ψ is the wavelet transform. As can be seen from Fig. 5, the wavelet domain contains a small, low-resolution rendition of the full MR image in the upper-left corner, whereas the remaining regions encode high spatial frequency details. By taking the l_1 norm on the wavelet transform, we emphasize much more the importance of the upper-left corner compared to the rest of the wavelet domain. In order words, in addition to ensuring data consistency in *k*-space via the first half of Eq. 3, the second half ensures we fit not to localized fluctuations and noise but, rather, to the global pattern across the entire image.

k-t *SPARSE and* k-t *SPARSE-SENSE*

The first compressed sensing sequence developed for dynamic MRI was *k-t SPARSE*.[31] Lustig et al[31] proposed that *k-t* space be undersampled pseudorandomly in a Cartesian manner (Fig. 6a). This sampling is performed using CINE acquisition; data are acquired over multiple cardiac cycles and rebinned postscan. Note that Fig. 6a illustrates a complete *k*-space slice after rebinning. They applied the wavelet transform in the spatial domain and the Fourier transform along the temporal domain to sparsify their data. Acceleration up to 5-fold was achieved for brain imaging and 3D MR angiography. In a variation of this technique, parallel imaging was incorporated to increase acceleration in a technique called *k-t* SPARSE-SENSE.[32] The authors demonstrated their technique on cardiac CINE datasets and made two adaptations to *k-t* SPARSE: including a sensitivity-encoding matrix *S* in the data consistency term, and using temporal total variation as the sparsity transform. With these changes, *k-t* SPARSE-SENSE showed significant improvements over its predecessor, both in reconstruction quality and acceleration (up to 8-fold acceleration).

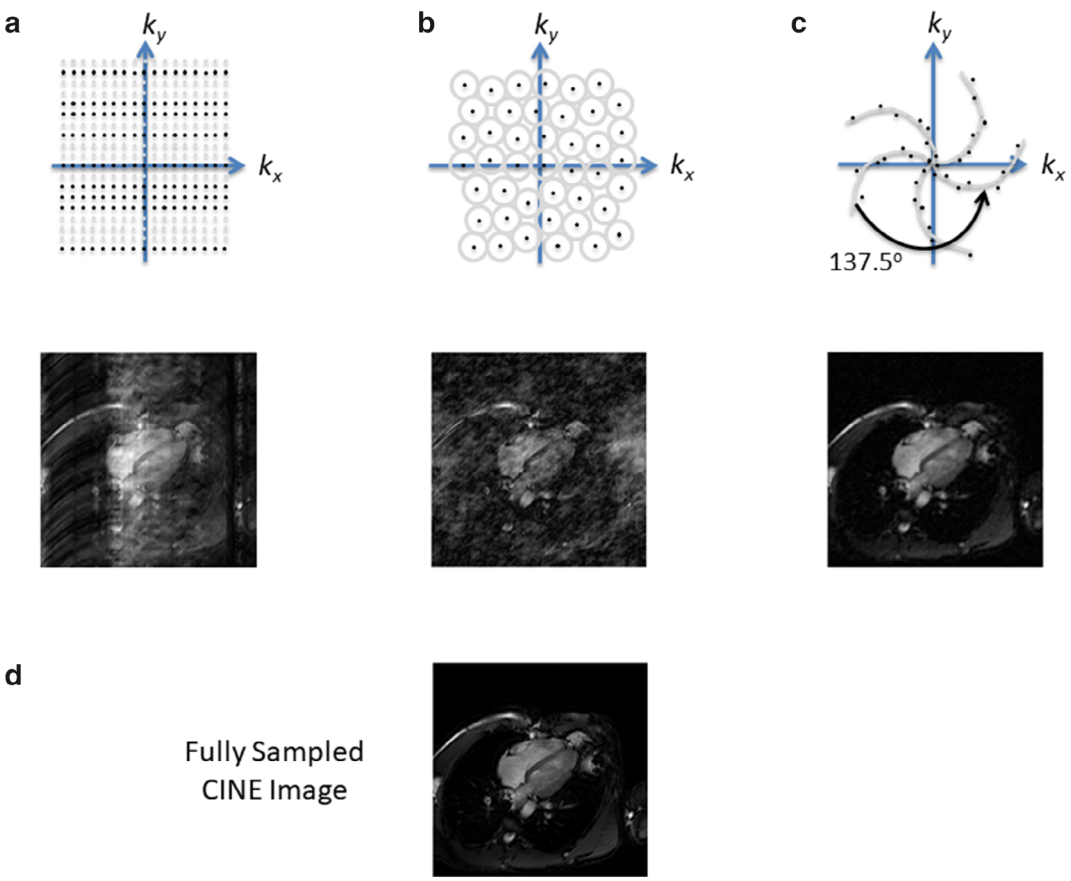

FIGURE 6: Random undersampling patterns used in compressed sensing. Random Cartesian undersampling for one frame of *k-t* space (a). Phase encode lines are chosen at random, but the frequency encode direction is fully sampled. VDPoisson random undersampling for one frame of *k-t* space (b). Acquired points are randomly selected according to a minimum distance metric (denoted by grey circles), which is selected using a Poisson probability distribution. VDRad random undersampling for one frame of*k-t*space (c). Random undersampling is based on predefined spiral trajectories, which are separated by 137.5° (shown by arrow). Reconstruction from fully sampled *k*-space shown for comparison (d).

k-t *FOCUSS*

k-t focal underdetermined system solver (FOCUSS) is a technique that unifies compressed sensing and *k-t* BLAST.[33] In fact, *k-t* BLAST is a special case of *k-t* FOCUSS. In *k-t* FOCUSS, one begins with a low-resolution estimate of a sparse signal in *x-f* space, which can be obtained from low-frequency *k-t* samples or training data. Through an iterative process, this solution is pruned to a sparse signal representation. Mathematically, *k-t* BLAST is simply the first iteration of *k-t* FOCUSS. However, unlike *k-t* BLAST, *k-t* FOCUSS minimizes the l_1 norm that is optimal for compressed sensing. When applied to cardiac CINE imaging, *k-t* FOCUSS demonstrated acceptable image quality at acceleration factors up to 16.

Selecting the Sparsity Transform

A key focus of compressed sensing research is selection of an appropriate sparsity transform for a given application in order to ensure that accurate reconstructions are obtained.[34,35] In *k-t* SPARSE, the discrete cosine transform (DCT) and wavelet transform were compared in their role as sparsity transforms.[31] The wavelet transform was shown to outperform DCT, as 2D or 3D wavelets provide very high compression for natural images. As such, wavelet transforms are commonly used for compressed sensing procedures. Total variation (TV) has also been used, although its use is limited to static tissue, as TV cannot adequately capture edges or dynamic tissue.[34,36] This problem is addressed using total generalized variation (TGV), a higher-order extension of TV.[37] PCA has also been proposed as a potential sparsity transform for dynamic tissue and has shown promise in accelerating phase-contrast CINE MRI.[38] Lastly, patch-based sparsity transforms have been used, offering a balance between local and global patterns present within an image.[39]

Improving the Undersampling Pattern

We have seen Cartesian undersampling strategies via *k*-t SPARSE/*k*-t SENSE. However, a limitation of implementing randomness within a Cartesian sampling framework is that the aliasing artifacts in the image domain are coherent to a certain extent. Because only true random undersampling produces incoherent artifacts,[40] non-Cartesian pseudorandom acquisition strategies that resemble true random undersampling are desirable for compressed sensing MRI. Another consideration is SNR degradation: non-Cartesian pseudorandom acquisition strategies should prioritize the center of *k*-space.[41] One such undersampling strategy is variable density Poisson (VDPoisson)[42] was designed to approximate true random undersampling but maintain a fixed minimum distance between sample points (Fig. 6b). This fixed distance is chosen using the Poisson distribution, hence the name VDPoisson. This undersampling was performed using CINE acquisition; a single rebinned *k*-space is shown in Fig. 6b. In that study, the authors were able to achieve acceleration factors ranging from 4 to 6.3.[42] A second example is variable density sampling and radial view ordering (VDRad),[43] which was designed to improve coverage of the central *k*-space region (Fig. 6c). It shows similarities to the work of Prieto et al,[24] who defined spirals trajectories separated by the golden ratio. In VDRad, however, random undersampling occurs along these spirals. This undersampling was performed using CINE acquisition; a single rebinned *k*-space is shown in Fig. 6c. Since VDRad is designed to update the center of *k*-space, it is well suited for dynamic MRI applications. In that study, the authors reported an acceleration factor of ~6 for each cardiac phase.[43] A fully sampled CINE image is also shown for comparison (Fig. 6d).

Improving the Acceleration Rate

In the examples discussed so far, we have seen that the acceleration factor gained by compressed sensing ranges from 4–16. However, if we combined compressed sensing with low-rank reconstruction (ie, using fewer dimensions to represent high-dimensional data), higher acceleration factors can be achieved without degrading reconstruction quality. For example, a time-series in MRI possesses strong correlation over time, which means that missing *k-t* space data points can be estimated using low-rank matrix completion, such as *k-t* sparsity and low-rank structure.[44] Low-rank approaches can also be integrated with a sparse decomposition for regularization, as in *k-t* robust principal component analysis for dynamic MRI.[45] *k-t* RPCA separates the low-rank component, which accounts for slow time-varying behavior (eg, background image) from the sparsity component, which captures abrupt changes (eg, motion, dynamic contrast enhancement). When motion is present, both *k-t* SLR and *k-t* RPCA outperform *k-t* FOCUSS at various acceleration factors.[44,45] It is worth noting that while *k-t* SLR and *k-t* RPCA are not strictly compressed sensing, at their core they involve numerical optimization, which is fundamental to compressed sensing reconstruction.

Summary

Compressed sensing revolutionized accelerated cardiac MRI and many other applications beyond the scope of this review, such as angiography, functional MRI, relaxometry, and arterial spin labeling.[46–49] It provided a method for an accurate reconstruction of undersampled acquired *k-t* space data, a feat *k-t* accelerated imaging could not guarantee. Compressed sensing has now seen clinical implementation. Siemens MR scanners (Erlangen, Germany) are capable of using compressed sensing reconstruction to achieve a temporal resolution of 48 msec,[50,51] and Philips MR scanners (Best, Netherlands) offer a reduction in total scan time by a factor of 2.[52] However, a few limitations remain: long reconstruction times, the need to tune parameters, and the masking of

possibly relevant local information via the sparsity transform. We explore in the final section how deep learning has partly overcome these hurdles.

Deep Learning

While *k-t* acceleration and compressed sensing have revolutionized the field of rapid MRI in the past two decades, reconstructing high-quality images at a temporal resolution less than 33 msec (~30 frames per second) still remains an important consideration in rapid MRI. A key bottleneck to achieving higher acceleration is finding robust methods for nonlinear reconstruction. Recognizing this limitation, an increasing number of researchers have recently turned to artificial intelligence, or, more accurately, deep-learning methods, to learn the nonlinear optimization. Rather than explicitly define an analytical model, deep learning relies on training data to learn the model and the unknown solution it produces.

Deep-learning-based reconstruction, like previous methods, is an exercise in solving an inverse problem. That is, given an observed signal k in k-space, which is the output of our system E, we want to determine the input signal x (in our case, an MR image). With analytical techniques, finding the inverse solution is formulated as a regularized optimization problem:

$$\hat{x} = \underset{x}{\operatorname{argmin}} \|Ex - k\|_2^2 + \lambda \Phi(x) \tag{4}$$

where the reconstructed image $\hat{x}$ is estimated by minimizing a data consistency term $\|Ex-k\|_2^2$, where x is the ground truth image, and a regularization term $\lambda\Phi(x)$. In compressed sensing, tuning the sparsifying transform $\Phi(x)$ and regularization parameters is required for different types of MR images, which is challenging and time-consuming. Deep learning uses an alternative approach to solving the inverse problem. The data consistency term specified in Eq. 4 is replaced with $\left\|g_\varphi(k) - x\right\|_2^2$, where $g_\varphi(\cdot)$ is a convenient function that acts as E^{-1} and φ are trainable parameters of the neural network. This optimization is simple and efficient, allowing a direct mapping of acquired k-space data k to the reconstructed image $\hat{x}$ via $\hat{x} = g_\varphi(k)$. Once the network parameters φ are learned, MR images can be reconstructed approximately twice as fast as clinical compressed sensing protocols[50–53]—the key advantage of deep learning over previous approaches.

Neural Network Architecture

The convolutional neural network (CNN) is the most common class of deep neural networks implemented for image analysis. CNNs exploit the spatial–temporal coherencies that exist in most natural images, including medical images, and apply a small kernel filter (eg, 3×3, 5×5, or 7×7 pixel mask) over different areas of an image to extract different features (eg, vertical edge, diagonal edge, etc.), storing those features in the next "layer" called a feature map. These feature maps are nothing more than spatially localized image features and, in conventional CNNs, have the same dimensions as the original image; the number of feature maps is equal to the number of different filters applied to the image. The feature maps are then fed to the next (ie, deeper) layer, where the convolution process repeats and another set of filters are applied for higher abstraction. At increasing depths, features become more complex, evolving from edges to shapes to even more global, complicated patterns we do not entirely understand to this day. What we do know is that deeper networks generally produce significantly better-quality results compared to shallow networks, as more contextual information is captured with each additional layer.

In a variation of the conventional CNN known as an encoder-decoder network, or U-Net,[54] we spatially downsample feature maps through pooling (max pooling or average pooling), in which only the maximum or average value in a neighborhood of, say, 2×2 pixels is retained, thereby reducing the dimension of the feature map by a factor of 2 in both the vertical and horizontal directions. This way, the size of the feature maps is reduced at each convolution step until the bottleneck layer is reached, at which point upsampling is performed until we retrieve the original image size. The downsampling operation effectively forces a "compressed" or abstract representation of the input to be learned. However, high-resolution details can be lost through this approach. One remedy is to include skip connections to preserve relevant details. See Fig. 7 for a schematic of a U-Net.

Note that the convolution operation at each layer is simply a linear combination, where the input vector corresponding to neighboring image pixels are multiplied point-by-point with filter weights and then summed to produce an output value at a location in the feature map. The task of training the CNN, therefore, is to learn the optimal filter weights such that the most relevant features are extracted via convolution. This optimization is conducted by minimizing a loss function through training the CNN on an abundance of input data (ie, MR images from undersampled k-space acquisitions) and comparing these against a ground truth (ie, true MR images from full k-space reconstruction). Training can be broken up into multiple steps, where the network parameters φ are updated each step via a gradient descent algorithm.[55] This update is dictated by the loss function; hence, the choice of an appropriate loss function is critical. We have already seen the mean squared error (MSE), or squared l_2 norm, conventionally employed for the loss function. However, other loss functions have also been adopted, such as the l_1 norm and, increasingly, the structural similarity index.[56] The latter metric more closely mimics our

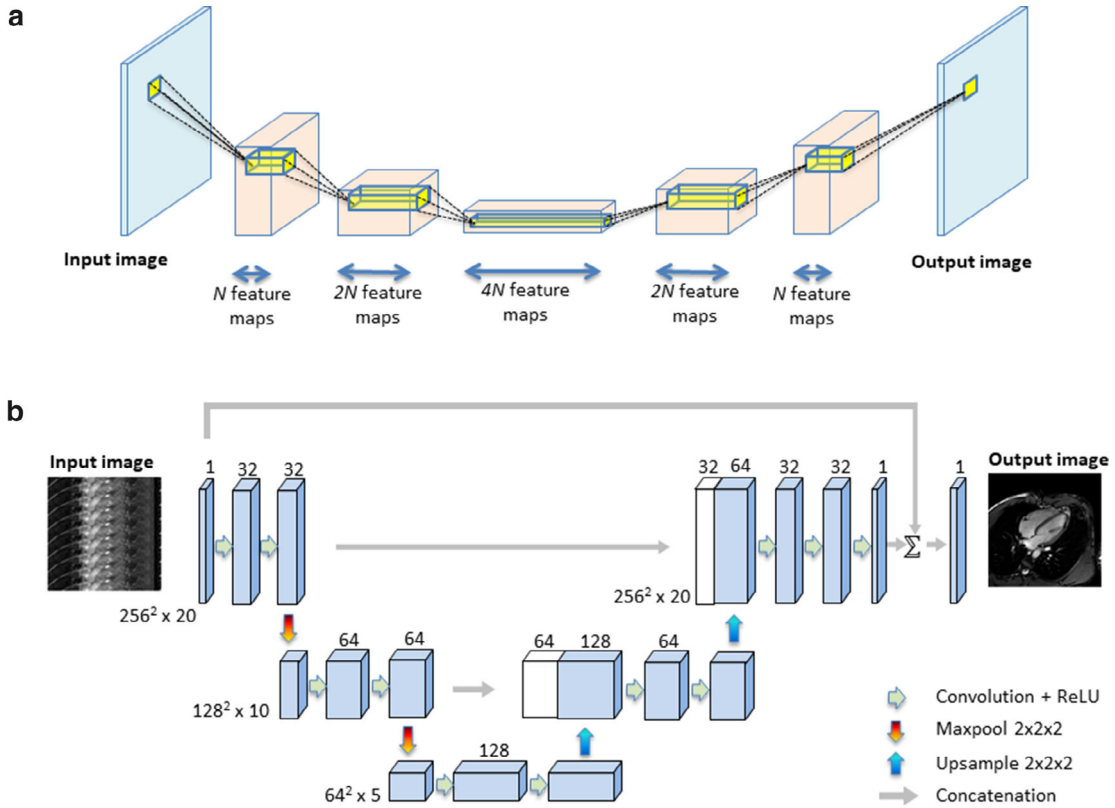

FIGURE 7: U-Net CNN architecture. (a) In the U-Net CNN, the encoding half spatially compresses feature maps by spatially downsampling, while the decoding half upsamples back to the original image size. The yellow prisms represent the convolution process that takes information from one layer (eg, image) to feature maps in the next layer. (b) An illustration of U-Net applied to MRI cardiac MRI reconstruction, using a 20-frame 256 × 256 stack of images as an example. Unaliased images from undersampling are fed as input to the U-Net. Gray arrows represent skip connections

visual perception of structure and content and does not enforce pixelwise agreement.

Deep Learning Applications for Cardiac MRI Reconstruction

We summarize herein key developments in the application of deep learning to accelerated MRI reconstruction. Some noncardiac applications are necessarily included, but topics pertaining to segmentation, localization, tissue characterization, and disease prognosis are not reviewed; the reader is referred to Leiner et al for details on these other topics.[57]

In 2016, Wang et al[58] reported one of the first applications of deep learning to reconstructing MR images. Zero-filled *k*-space data transformed to the image domain were given as training input data to a fully-connected three-layer CNN; by retaining predominantly lower-frequency *k*-space, the authors were able to reconstruct high-fidelity brain MR images up to an acceleration factor of 5. In 2018, Hyun et al[59] adopted a U-Net architecture, again for reconstructing brain MR images; they showed that by retaining only 29% of *k*-space data, images with quality similar to those from full *k*-space reconstruction could be obtained. In the years since, implementation of the U-Net architecture has grown exponentially.[60]

In 2018, Schlemper et al[53] presented the first demonstration of dynamic cardiac MR reconstruction using a deep CNN. Like their predecessors, they demonstrated that the key information was contained predominantly in the central region of *k*-space and that zero-filled *k*-space transformed to noisy images could be fed as input for training the neural network. Because they were working with a time-series, the authors introduced data-sharing across time (Fig. 8) to achieve further acceleration, up to a factor of 11, and outperforming state-of-the-art compressed sensing reconstruction. A variation by the same group was published in 2019,[61] where a recurrent CNN, which is much more compact than conventional CNN cascades, was implemented for reconstructing undersampled dynamic cardiac MR data.

In all of the above deep-learning strategies, the Fourier relationship is an integral part of the training, because the Fourier transform is explicitly applied to acquired *k*-space data to produce MR images as input to the neural network. However, what if we did not specify the transform relationship but, instead, allowed the neural network to directly learn the transformation between the sensor domain (ie, *k*-space) and the output image domain? This concept was proposed by Zhu et al in 2018, who described a framework for generalized reconstruction called AUTOMAP.[62] The architecture is

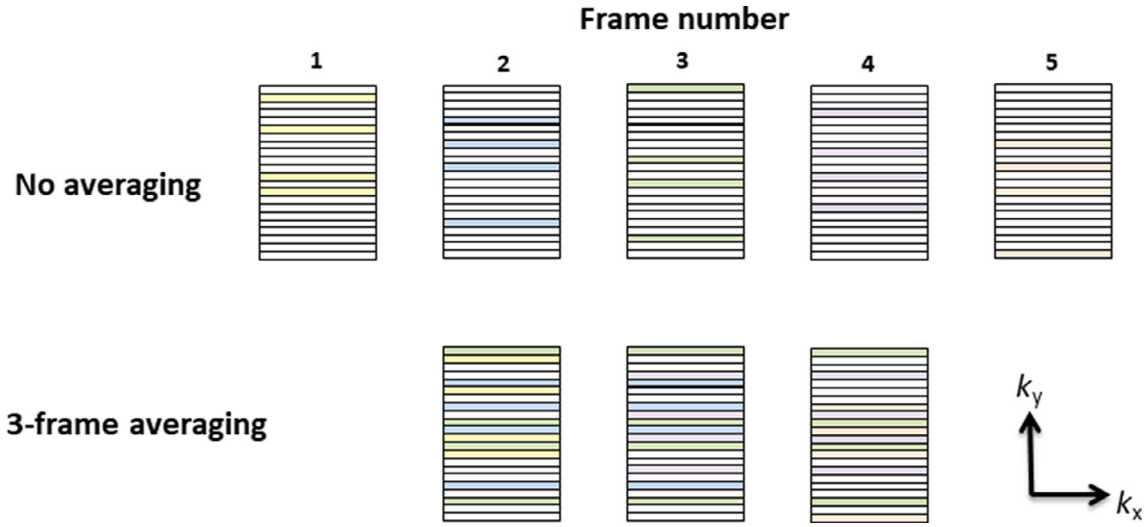

FIGURE 8: Data-sharing for time-series. Each time frame is undersampled differently; colored lines represent acquired phase-encode lines. When averaging is employed, the missing phase-encode lines are filled in using values from *n* contiguous time frames, where *n* = 3 in this example. Overlapping lines are averaged.

comprised of feed-forward, fully connected layers followed by a sparse convolutional autoencoder. What is unique with this approach is that it does not implement a specific image reconstruction task. In fact, the network can be trained on image-Fourier pairs of animals and plants and still accurately reconstruct brain MR images.[62] However, AUTOMAP is computationally expensive, with the number of parameters scaling quadratically with the input size. A mitigation strategy was later proposed by Schlemper et al via decomposed AUTOMAP, or dAUTOMAP, which takes advantage of the linear separability of the 2D Fourier kernel to make AUTOMAP scalable.[63] By virtue of training fewer parameters and reducing the likelihood of overfitting, dAUTOMAP was shown to outperform AUTOMAP for cardiac MR reconstruction, notably by preserving high-frequency details that tend to be oversmoothed by AUTOMAP.

Summary

Deep learning is a relatively new technique, not only in cardiac MRI but in image reconstruction in general. Yet it has already demonstrated immense potential for analysis of high-dimensional datasets and real-time reconstruction. It has even seen applications beyond rapid cardiac CINE MRI, such as accelerated 5D MRI reconstruction,[64] MR perfusion,[65] MR relaxometry,[66] dynamic contrast-enhanced MRI,[67] and MR fingerprinting.[68,69] Furthermore, one should note that while deep learning *allows* for any arbitrary undersampling pattern, certain undersampling patterns will outperform others. This flexibility is a significant advantage over the constraint of pseudorandomness with compressed sensing. Despite these advantages, there are notable limitations on using neural networks to solve the inverse problem in imaging. One key limitation is that the knowledge acquired by the network is as good as the data on which it is trained. Not only is there a lack of voluminous cardiac MRI datasets in the public domain for training, but there is also the issue of differences in scanner hardware, sequences, imaging parameters, and so forth, which amounts to a generalizability issue that remains open to investigation. Furthermore, as was the case with compressed sensing, deep learning also has the potential to mask possibly relevant local information. For instance, important local physiological perturbations may be interpreted as artifacts and subsequently removed in the reconstructed image. Perhaps a more profound question to ask is whether too much hope has been placed on deep networks, which to this day remain very much a "black box." After all, we already possess a great deal of understanding of the inverse problem and the analytical tools to solve it. Injecting these analytical tools into a neural network could help address this issue, and may be an avenue for future exploration.

Conclusion

Innovations for accelerated cardiac MRI and dynamic MRI have evolved dramatically over the past three decades, initially drawing on hardware and mathematical ingenuity to reap gains in acceleration and, most recently, on deep neural networks to learn patterns elusive to human perception. Every solution presented its own benefits and drawbacks. Hardware techniques, for instance, were the simplest to understand from a mathematical perspective but were limited in reconstruction quality and acceleration. *k-t* accelerated imaging was able to improve on reconstruction quality but, nonetheless, could not provide a strict guarantee of reconstruction accuracy. Compressed sensing was able to improve reconstruction accuracy, but its theoretical underpinning imposed constraints on both the undersampling strategy and the reconstruction speed. Deep learning has shown similar or better

reconstruction quality as compressed sensing with flexible undersampling strategies and much faster reconstruction speed. Our historical review not only examined the crux of key acceleration methods for cardiac CINE MRI but, more importantly, provided the contextual link as to why one innovation led to the next. Hopefully, the reader has gained a holistic appreciation of both successes and unresolved challenges in accelerated cardiac CINE MRI.

REFERENCES

1. Cardiovascular diseases (CVDs) [https://www.who.int/en/news-room/fact-sheets/detail/cardiovascular-diseases-(cvds)]
2. Paterson I, Mielniczuk LM, O'Meara E, So A, White JA. Imaging heart failure: Current and future applications. Can J Cardiol 2013;29:317-328.
3. Axel L, Otazo R. Accelerated MRI for the assessment of cardiac function. Br J Radiol 2016;89:20150655.
4. Malik SB, Chen N, Parker RA 3rd, Hsu JY. Transthoracic echocardiography: Pitfalls and limitations as delineated at cardiac CT and MR imaging. Radiographics 2017;37:383-406.
5. Plewes DB, Kucharczyk W. Physics of MRI: A primer. J Magn Reson Imaging 2012;35:1038-1054.
6. Ghugre NR, Pop M, Barry J, Connelly KA, Wright GA. Quantitative magnetic resonance imaging can distinguish remodeling mechanisms after acute myocardial infarction based on the severity of ischemic insult. Magn Reson Med 2013;70:1095-1105.
7. Tseng W-YI SM-YM, Tseng Y-HE. Introduction to cardiovascular magnetic resonance: Technical principles and clinical applications. Acta Cardiol Sin 2016;32:129-144.
8. Pennell DJ. Cardiovascular magnetic resonance. Circulation 2010;121:692-705.
9. Rajiah P, Bolen MA. Cardiovascular MR imaging at 3 T: Opportunities, challenges, and solutions. Radiogr A Rev Publ Radiol Soc North Am Inc 2014;34:1612-1635.
10. Uecker M, Zhang S, Voit D, Karaus A, Merboldt KD, Frahm J. Real-time MRI at a resolution of 20 msec. NMR Biomed 2010;23:986-994.
11. Kellman P, Chefd'hotel C, Lorenz CH, Mancini C, Arai AE, McVeigh ER. High spatial and temporal resolution cardiac cine MRI from retrospective reconstruction of data acquired in real time using motion correction and resorting. Magn Reson Med 2009;62:1557-1564.
12. Xue H, Kellman P, Larocca G, Arai AE, Hansen MS. High spatial and temporal resolution retrospective cine cardiovascular magnetic resonance from shortened free breathing real-time acquisitions. J Cardiovasc Magn Reson 2013;15:102.
13. Waterton JC, Jenkins JP, Zhu XP, Love HG, Isherwood I, Rowlands DJ. Magnetic resonance (MR) cine imaging of the human heart. Br J Radiol 1985;58:711-716.
14. Ridgway JP. Cardiovascular magnetic resonance physics for clinicians: Part I. J Cardiovasc Magn Reson 2010;12:71.
15. Krishnamurthy R, Cheong B, Muthupillai R. Tools for cardiovascular magnetic resonance imaging. Cardiovasc Diagn Ther 2014;4:104-125.
16. Kemp CD, Conte JV. The pathophysiology of heart failure. Cardiovasc Pathol 2012;21:365-371.
17. Griswold MA, Jakob PM, Nittka M, Goldfarb JW, Haase A. Partially parallel imaging with localized sensitivities (PILS). Magn Reson Med 2000;44:602-609.
18. Pruessmann KP, Weiger M, Scheidegger MB, Boesiger P. SENSE: Sensitivity encoding for fast MRI. Magn Reson Med 1999;42:952-962.
19. Sodickson DK, Manning WJ. Simultaneous acquisition of spatial harmonics (SMASH): Fast imaging with radiofrequency coil arrays. Magn Reson Med 1997;38:591-603.
20. Griswold MA, Jakob PM, Heidemann RM, et al. Generalized autocalibrating partially parallel acquisitions (GRAPPA). Magn Reson Med 2002;47:1202-1210.
21. Heidemann RM, Griswold MA, Haase A, Jakob PM. VD-AUTO-SMASH imaging. Magn Reson Med 2001;45:1066-1074.
22. Winkelmann S, Schaeffter T, Koehler T, Eggers H, Doessel O. An optimal radial profile order based on the golden ratio for time-resolved MRI. IEEE Trans Med Imaging 2007;26:68-76.
23. Arif O, Afzal H, Abbas H, Amjad MF, Wan J, Nawaz R. Accelerated dynamic MRI using kernel-based low rank constraint. J Med Syst 2019;43:271.
24. Prieto C, Doneva M, Usman M, et al. Highly efficient respiratory motion compensated free-breathing coronary MRA using golden-step Cartesian acquisition. J Magn Reson Imaging 2015;41:738-746.
25. Huang F, Akao J, Vijayakumar S, Duensing GR, Limkeman M. K-t GRAPPA: A k-space implementation for dynamic MRI with high reduction factor. Magn Reson Med 2005;54:1172-1184.
26. Riederer SJ, Tasciyan T, Farzaneh F, Lee JN, Wright RC, Herfkens RJ. MR fluoroscopy: Technical feasibility. Magn Reson Med 1988;8:1-15.
27. Madore B, Glover GH, Pelc NJ. Unaliasing by Fourier-encoding the overlaps using the temporal dimension (UNFOLD), applied to cardiac imaging and fMRI. Magn Reson Med 1999;42:813-828.
28. Rosenfeld D. New approach to gridding using regularization and estimation theory. Magn Reson Med 2002;48:193-202.
29. Tsao J, Boesiger P, Pruessmann KP. k-t BLAST and k-t SENSE: Dynamic MRI with high frame rate exploiting spatiotemporal correlations. Magn Reson Med 2003;50:1031-1042.
30. Pedersen H, Kozerke S, Ringgaard S, Nehrke K, Kim WY. k-t PCA: Temporally constrained k-t BLAST reconstruction using principal component analysis. Magn Reson Med 2009;62:706-716.
31. Lustig M, Donoho D, Pauly JM. Sparse MRI: The application of compressed sensing for rapid MR imaging. Magn Reson Med 2007;58:1182-1195.
32. Feng L, Srichai MB, Lim RP, et al. Highly accelerated real-time cardiac cine MRI using k-t SPARSE-SENSE. Magn Reson Med 2013;70:64-74.
33. Jung H, Ye JC, Kim EY. Improved k-t BLAST and k-t SENSE using FOCUSS. Phys Med Biol 2007;52:3201-3226.
34. Feng L, Benkert T, Block KT, Sodickson DK, Otazo R, Chandarana H. Compressed sensing for body MRI. J Magn Reson Imaging 2017;45:966-987.
35. Bustin A, Fuin N, Botnar RM, Prieto C. From compressed-sensing to artificial intelligence-based cardiac MRI reconstruction. Front Cardiovasc Med 2020;7:17.
36. Abascal JFPJ, Montesinos P, Marinetto E, Pascau J, Desco M. Comparison of total variation with a motion estimation based compressed sensing approach for self-gated cardiac cine MRI in small animal studies. PLoS One 2014;9:e110594.
37. Schloegl M, Holler M, Schwarzl A, Bredies K, Stollberger R. Infimal convolution of total generalized variation functionals for dynamic MRI. Magn Reson Med 2017;78:142-155.
38. Kim D, Dyvorne HA, Otazo R, Feng L, Sodickson DK, Lee VS. Accelerated phase-contrast cine MRI using k-t SPARSE-SENSE. Magn Reson Med 2012;67:1054-1064.
39. Yoon H, Kim KS, Kim D, Bresler Y, Ye JC. Motion adaptive patch-based low-rank approach for compressed sensing cardiac cine MRI. IEEE Trans Med Imaging 2014;33:2069-2085.
40. Donoho DL. Compressed sensing. IEEE Trans Inf Theory 2006;52:1289-1306.
41. Geethanath S, Reddy R, Konar AS, et al. Compressed sensing MRI: A review. Crit Rev Biomed Eng 2013;41:183-204.
42. Vasanawala SS, Alley MT, Hargreaves BA, Barth RA, Pauly JM, Lustig M. Improved pediatric MR imaging with compressed sensing. Radiology 2010;256:607-616.

43. Cheng JY, Zhang T, Ruangwattanapaisarn N, et al. Free-breathing pediatric MRI with nonrigid motion correction and acceleration. J Magn Reson Imaging 2015;42:407-420.

44. Lingala SG, Hu Y, DiBella E, Jacob M. Accelerated dynamic MRI exploiting sparsity and low-rank structure: k-t SLR. IEEE Trans Med Imaging 2011;30:1042-1054.

45. Tremoulheac B, Dikaios N, Atkinson D, Arridge SR. Dynamic MR image reconstruction-separation from undersampled (k,t)-space via low-rank plus sparse prior. IEEE Trans Med Imaging 2014;33:1689-1701.

46. Stalder AF, Schmidt M, Quick HH, et al. Highly undersampled contrast-enhanced MRA with iterative reconstruction: Integration in a clinical setting. Magn Reson Med 2015;74:1652-1660.

47. Jeromin O, Pattichis MS, Calhoun VD. Optimal compressed sensing reconstructions of fMRI using 2D deterministic and stochastic sampling geometries. Biomed Eng Online 2012;11:25.

48. Bai R, Cloninger A, Czaja W, Basser PJ. Efficient 2D MRI relaxometry using compressed sensing. J Magn Reson 2015;255:88-99.

49. Taso M, Zhao L, Guidon A, Litwiller DV, Alsop DC. Volumetric abdominal perfusion measurement using a pseudorandomly sampled 3D fast-spin-echo (FSE) arterial spin labeling (ASL) sequence and compressed sensing reconstruction. Magn Reson Med 2019;82:680-692.

50. Forman C, Wetzl J, Hayes C, Schmidt M. Compressed sensing: A paradigm shift in MRI. MAGNETOM Flash 2016;66:8–13.

51. Liu J, Rapin J, Chang T, et al.: Dynamic cardiac MRI reconstruction with weighted redundant Haar wavelets. In: Proc 20th Annual Meeting ISMRM, Melbourne, Australia; 2012.

52. Geerts-Ossevoort L, De Weerdt E, Duijndam A, et al. Compressed SENSE speed done right. Every time. Philips FieldStrength Mag 2018; 1–14.

53. Schlemper J, Caballero J, Hajnal JV, Price AN, Rueckert D. A deep cascade of convolutional neural networks for dynamic MR image reconstruction. IEEE Trans Med Imaging 2018;37:491-503.

54. Ronneberger O, Fischer P, Brox T. U-Net: Convolutional Networks for Biomedical Image Segmentation. In: Navab N, Hornegger J, Wells W, Frangi A. (eds) Medical Image Computing and Computer-Assisted Intervention – MICCAI 2015. MICCAI 2015. Lecture Notes in Computer Science, vol 9351. Springer. 2015.

55. Watt J, Borhani R, Katsaggelos AK. *Machine learning refined: Foundations, algorithms, and applications*. Cambridge, UK: Cambridge Universitiy Press; 2016.

56. Wang Z, Bovik AC, Sheikh HR, Simoncelli EP. Image quality assessment: From error visibility to structural similarity. IEEE Trans Image Process 2004;13:600-612.

57. Leiner T, Rueckert D, Suinesiaputra A, et al. Machine learning in cardiovascular magnetic resonance: Basic concepts and applications. J Cardiovasc Magn Reson 2019;21:61.

58. Wang S, Su Z, Ying L, et al. Accelerating magnetic resonance imaging via deep learning. In: Proceedings IEEE Int Symp Biomed Imaging 2016;2016:514-517.

59. Hyun CM, Kim HP, Lee SM, Lee S, Seo JK. Deep learning for undersampled MRI reconstruction. Phys Med Biol 2018;63:135007.

60. Bahadir CD, Wang AQ, Dalca AV, Sabuncu MR. Deep-learning-based optimization of the under-sampling pattern in MRI. IEEE Trans Comput Imaging 2020;6:1139-1152.

61. Qin C, Schlemper J, Caballero J, Price AN, Hajnal JV, Rueckert D. Convolutional recurrent neural networks for dynamic MR image reconstruction. IEEE Trans Med Imaging 2019;38:280-290.

62. Zhu B, Liu JZ, Cauley SF, Rosen BR, Rosen MS. Image reconstruction by domain-transform manifold learning. Nature 2018;555:487-492.

63. Schlemper J, Oksuz I, Clough J, et al. dAUTOMAP: decomposing AUTOMAP to achieve scalability and enhance performance. arXiv 2019;1909.10995v2.

64. Chen Y, Shaw JL, Xie Y, Li D, Christodoulou AG. Deep learning within a priori temporal feature spaces for large-scale dynamic MR image reconstruction: Application to 5-D cardiac MR multitasking. Lect Notes Comput Sci 2019;1910.00956v1.

65. Fan L, Shen D, Haji-Valizadeh H, et al. Rapid dealiasing of undersampled, non-Cartesian cardiac perfusion images using U-net. NMR Biomed 2020;33:e4239.

66. Cao P, Liu J, Tang S, et al. Technical note: Simultaneous segmentation and relaxometry for MRI through multitask learning. Med Phys 2019; 46:4610-4621.

67. Feng L, Wen Q, Huang C, Tong A, Liu F, Chandarana H. GRASP-Pro: imProving GRASP DCE-MRI through self-calibrating subspace-modeling and contrast phase automation. Magn Reson Med 2020;83: 94-108.

68. Fang Z, Chen Y, Liu M, et al. Deep learning for fast and spatially constrained tissue quantification from highly accelerated data in magnetic resonance fingerprinting. IEEE Trans Med Imaging 2019;38:2364-2374.

69. Chen Y, Fang Z, Hung SC, Chang WT, Shen D, Lin W. High-resolution 3D MR fingerprinting using parallel imaging and deep learning. Neuroimage 2020;206:116329.